

A Visual-inertial Navigation Method for High-Speed Unmanned Aerial Vehicles

Xin-long Luo ^{a 1}, Jia-hui Lv ^a and Geng Sun ^b

^a School of Information and Communication Engineering,
Beijing University of Posts and Telecommunications, P. O. Box 101,
Xitucheng Road No. 10, Haidian District, 100876, Beijing China
luoxinlong@bupt.edu.cn, jhlv@bupt.edu.cn

^bInstitute of Mathematics, Academy of Mathematics and Systems Science,
Chinese Academy of Sciences, 100190, Beijing China
sung@amss.ac.cn

Abstract

This paper investigates the localization problem of high-speed high-altitude unmanned aerial vehicle (UAV) with a monocular camera and inertial navigation system. And it proposes a navigation method utilizing the complementarity of vision and inertial devices to overcome the singularity which arises from the horizontal flight of UAV. Furthermore, it modifies the mathematical model of localization problem via separating linear parts from nonlinear parts and replaces a nonlinear least-squares problem with a linearly equality-constrained optimization problem. In order to avoid the ill-condition property near the optimal point of sequential unconstrained minimization techniques (penalty methods), it constructs a semi-implicit continuous method with a trust-region technique based on a differential-algebraic dynamical system to solve the linearly equality-constrained optimization problem. It also analyzes the global convergence property of the semi-implicit continuous method in an infinity integrated interval other than the traditional convergence analysis of numerical methods for ordinary differential equations in a finite integrated interval. Finally, the promising numerical results are also presented.

Keywords: vision odometry, monocular camera, unmanned aerial vehicle, differential-algebraic gradient flow, semi-implicit continuation method, trust-region technique

AMS subject classifications. 65H17, 65J15, 65K05, 65L05

1. Introduction

Localization is essential for autonomous navigation of unmanned aerial vehicles. In terms of aircraft navigation, the aircraft usually uses an inertial integrated navigation method to guide flight due to the unsatisfactory effect of pure inertial navigation system (INS) (see [33]). The visual-based navigation method has received widespread

attention in recent years for its great performance in this field. Therefore, we utilize visual odometer which is complementary to inertial measurement to assist INS.

Visual-based methods are often applied in low speed and low height situations, resulting from such drawback as motion blur. Being different from others, our work tries to solve the localization problem of high-speed unmanned aerial vehicles (UAVs) in high altitude. In order to overcome the motion blur and scale ambiguity that arise in this challenging practical problem, a novel visual based method combining the inertial navigation system is designed.

In the case of challenging camera dynamics, the imaging of landmarks inevitably appears blurred. According to the principle of pinhole imaging, we consider an additional error to the angle of view for the landmarks imaging and the optical center of camera lens, which is determined by the property of the camera. Note that the angular error has a great impact on the position estimation of the aircraft due to the extremely high flight altitude. For the scale ambiguity, rather than assume the homography, we use the altitude difference of the aircraft in a short time interval measured by altimeter to determine the height of aerial vehicle.

For a real engineering problem, a UAV flight trajectory is usually relatively simple. In particular, when a UAV flies on a horizontal plane, the flight altitude difference with reading error within a short time interval will be intensely small. Generally, that scenario leads to the singularity even using an altimeter to help determine scale. The singularity results in rapid accumulation of errors. In order to overcome its singularity, we add an inertial distance between two sequential frames to assist visual localization.

Furthermore, we modify the mathematical model of visual-inertial localization problem via separating linear parts from nonlinear parts and replace a nonlinear least-squares problem with a linearly equality-constrained optimization problem. In order to avoid the ill-condition property near the optimal point of sequential unconstrained minimization techniques (penalty methods [12, 30]), we construct a semi-implicit continuous method with a trust-region technique based on a differential-algebraic dynamical system to solve the linearly equality-constrained optimization problem. We also analyze the global convergence property of the proposed semi-implicit continuous method in an infinity integrated interval other than the traditional convergence analysis of numerical methods for ordinary differential equations in a finite integrated interval.

Finally, in order to validate the effectiveness of our proposed method, we adopt real parameters provided by China Aerospace Science and Industry Corporation to mimic the real flight environment and compare it with the pure inertial navigation method [36]. The simulation results show that our proposed method has better performance, and it meets the required accuracy in a long-term flight.

The rest of the paper is organized as follows. Firstly, we present the related work in section 2. Then, applied environment and sensors fusion architecture of our visual-inertial navigation method are described in section 3. In section 4, we modify the mathematical model and give a semi-implicit continuous method with a trust-region technique to solve that optimization problem. The simulation results of our method in comparison to the pure inertial navigation method are presented in section 5. Finally,

we give some discussions in section 6.

2. Related Work

In recent years, numerous methods have been applied to improve the precision of navigation. Among of navigation systems, the strap-down inertial navigation system (SINS) has great performance on pose estimation for its advantages of complete autonomy, strong anti-interference ability and high short-term precision [32, 14, 35]. However, the inertial measurement unit (IMU) which is the main component of SINS has an unavoidable cumulate error caused by sensor drifts [1, 11]. Therefore, many aerial vehicles utilize the position signal from GPS which fuses data generated by IMU to implement high navigation accuracy.

On the other hand, in many scenarios, GPS is difficult to play its role. In civil applications, GPS becomes inaccurate due to multipath effect as close to buildings and obstacles. In military field, such as ballistic missile vehicles, the position applications generally do not rely on GPS by reason of jamming and spoof [9]. In GPS denied environments, vision-based approach is an available and effective method, and visual-inertial odometer is ubiquitously applied on robots and unmanned aerial vehicles (UAVs) for its great performance of pose estimation and the complementarity between cameras and IMU [6, 7, 9, 10, 24, 26, 29, 38].

For the high altitude problem, we choose a monocular vision odometer to assist INS rather than the binocular camera, since the binocular camera reduces to a monocular camera when vehicles fly at high altitude as a result of the extremely small baseline-to-depth ratio [34]. If there is no additional information, scale ambiguity of a monocular camera can not be cleared up generally. Anwar et al. design a new depth-independent Jacobian matrix by relating the depth information with the area of region of interest [2]. In [7], Conte and Doherty consider the ground as flat and horizontal for aircraft flying at a relatively high altitude. Caballero et al. also assume the local ground flat but not level [8]. Both of them utilize planer homography to tackle the vehicle motion. In this paper, we give a method which does not require the local ground flat and does not rely on planar homography.

Zhang and Singh combine a high-accuracy INS and vision to estimate the position of a full-scale aircraft flying at an altitude of about 300 meters. They partially eliminate the effects of INS high-frequency noise through virtually rotating the camera parallel to local ground by reparametrizing features with their depth direction perpendicular to the ground [38]. Unlike Zhang and Singh, our method deal with the singular problem in the special case where the position of two frames have no altitude difference. In addition, we separate the nonlinear terms from the linear terms, and convert it to a linearly constrained optimization problem, rather than directly adopt the Levenberg-Marquardt method to solve nonlinear least-square problem. Furthermore, for that linearly equality-constrained optimization subproblem, we give a semi-implicit continuous method with a trust-region technique to solve it.

3. Sensors Fusion Architecture

In this paper, we focus our attention on the issue: solving the navigation problem of high speed and high altitude aircraft under the horizontal flight scenario. The navigation simulation is illustrated by Figure 1.

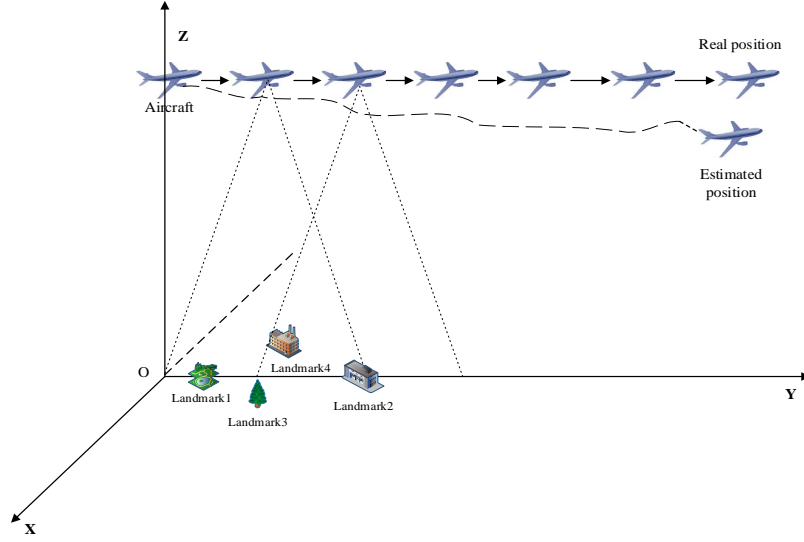


Figure 1: Navigation Simulation of Straight Line

The visual-inertial odometry, which is composed by a monocular vision system, an INS and an altimeter, is aimed to estimate the aircraft position and guide the flight of aerial vehicles. We consider the camera fitting a pinhole model briefly, and ignoring the lens distortion [15]. The Camera intrinsics parameters are given. As a convention, the 3D coordinate system denotes the real world as shown in Figure 1, and the symbol k , $k \in \mathbb{Z}^+$ denotes image frames. Besides the image coordinate system, another coordinate system is a 2D coordinate system with its origin being perpendicular to the optical center of camera lens, as shown in Figure 3. In the relatively difficult practical issue, velocity of the aircraft is between 200 meters per second and 300 meters per second, and the aerial vehicle flies at an altitude between 1000 meters and 1500 meters. Since the aerial vehicle flies with an extremely fast speed, the motion blur should be carefully considered. In order to reduce the influence of the blur, we use a camera to assist localization and add an angular error to the angle of view between camera and landmarks, about 0.2 degrees.

The sensor fusion architecture of the visual-inertial odometry is demonstrated in Figure 2. The odometer takes the camera images, altimeter reading from the altimeter and velocity from the INS. Combining those information, our method can acquire the vehicle position with low drift in the horizontal flight. When the aerial vehicle adjusts

its orientation, the angle of rotation is obtained by the IMU. Through acquiring the navigation information, reaching the destination along the scheduled route can be achieved with required accuracy.

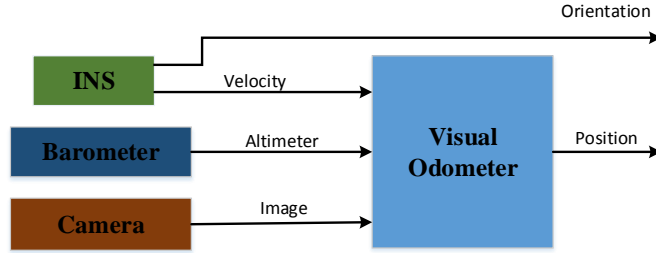


Figure 2: Sensor Fusion Architecture

In order to improve the navigation accuracy of ballistic missiles, we propose a method which utilizes monocular camera to assist the inertial navigation system. A monocular vision odometer typically has scale ambiguity. This scale ambiguity can be confirmed by the barometer through measuring the flying altitude. On the other hand, a vision odometer can suppress the cumulate error caused by IMU drift. Generally, taking full advantage of the complementarity of visual odometer and inertial navigation, the accuracy of navigation is improved.

4. Mathematical Model and Algorithm Descriptions

4.1. Mathematical Model

This subsection is aimed to illustrate the mathematical model of localization which is abstracted from practical problems. In that mathematical model, the positions of camera and landmarks are in the world coordinate. The sequence of frames is presented in parallel coordinate. Let the position of optical center in the k^{th} frame as (x_k, y_k, z_k) , and the $(k+1)^{th}$ frame as $(x_{k+1}, y_{k+1}, z_{k+1} + \delta h_k^{k+1})$, where δh_k^{k+1} is the height difference between two frames, obtained by an altimeter. The position of the n -th landmark, confirmed by ORB feature [27], is denoted as (x_{ln}, y_{ln}, z_{ln}) . We denote the location of the corresponding pixel imaged by the n^{th} landmark in the k^{th} frame as (x_{pn}^k, y_{pn}^k) . The vertical distance between the n^{th} landmark and the optical center of the camera of k^{th} frame is expressed as h_n^k . f_c is the focal length of the camera. The precedent notations are shown in Figure 3. Figure 3 presents the mathematic model of our visual odometer method appropriately.

This subsection shows the mathematical derivation of our proposed visual-inertial odometer method. In subsection 4.4, the complete algorithm is presented. From the model in Figure 3, we find the following relationships between the n^{th} landmark and

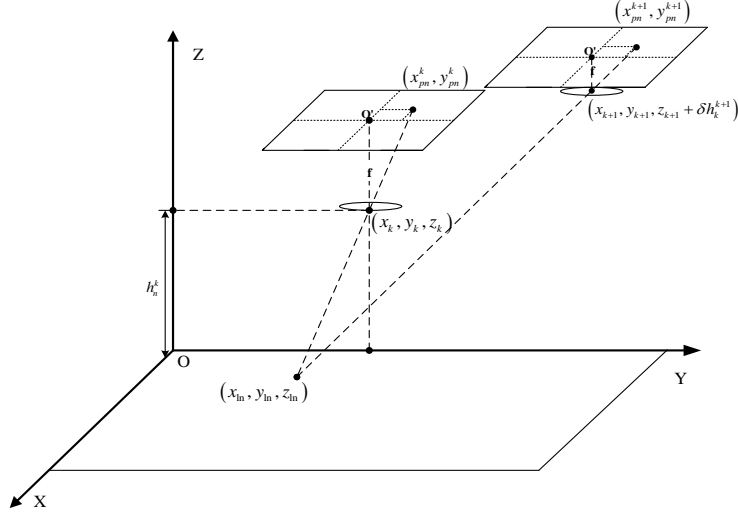


Figure 3: Mathematical model of visual-inertial odometer

the corresponding projection in two frames:

$$\begin{cases} \frac{x_k - x_{ln}}{h_n^k} = \frac{x_{pn}^k}{f_c}, \\ \frac{y_k - y_{ln}}{h_n^k} = \frac{y_{pn}^k}{f_c}, \\ \frac{x_{k+1} - x_{ln}}{h_n^k + \delta h_n^{k+1}} = \frac{x_{pn}^{k+1}}{f_c}, \\ \frac{y_{k+1} - y_{ln}}{h_n^k + \delta h_n^{k+1}} = \frac{y_{pn}^{k+1}}{f_c}. \end{cases} \quad (1)$$

The above relationship (1) is reformulated by

$$\begin{cases} x_{ln} + \frac{x_{pn}^k}{f_c} h_n^k = x_k, \\ y_{ln} + \frac{y_{pn}^k}{f_c} h_n^k = y_k, \\ x_{k+1} - x_{ln} - \frac{x_{pn}^{k+1}}{f_c} h_n^k = \frac{\delta h_n^{k+1}}{f_c} x_{pn}^{k+1}, \\ y_{k+1} - y_{ln} - \frac{y_{pn}^{k+1}}{f_c} h_n^k = \frac{\delta h_n^{k+1}}{f_c} y_{pn}^{k+1}. \end{cases} \quad (2)$$

In formula (2), the position of pixel in the camera coordinate and the position of the k^{th} frame are known, and the rest are unknown. Obviously, this is an underdetermined system and we can not determine the position of the next frame from equations (2). Therefore, we use more landmarks and more frames to determine the position of the next frame. In theory, we can obtain the solution by using only two landmarks. The

corresponding formula is shown as the following equations:

$$\begin{bmatrix} 0 & 0 & 1 & 0 & \frac{x_{p1}^k}{f} & 0 & 0 & 0 \\ 0 & 0 & 0 & 1 & \frac{y_{p1}^k}{f} & 0 & 0 & 0 \\ 1 & 0 & -1 & 0 & -\frac{x_{p1}^{k+1}}{f} & 0 & 0 & 0 \\ 0 & 1 & 0 & -1 & -\frac{y_{p1}^{k+1}}{f} & 0 & 0 & 0 \\ 0 & 0 & 0 & 0 & 0 & 1 & 0 & \frac{x_{p2}^k}{f} \\ 0 & 0 & 0 & 0 & 0 & 0 & 1 & \frac{y_{p2}^k}{f} \\ 1 & 0 & 0 & 0 & 0 & -1 & 0 & -\frac{x_{p2}^{k+1}}{f} \\ 0 & 1 & 0 & 0 & 0 & 0 & -1 & -\frac{y_{p2}^{k+1}}{f} \end{bmatrix} \begin{bmatrix} x_{k+1} \\ y_{k+1} \\ x_{l1} \\ y_{l1} \\ h_1^k \\ x_{l2} \\ y_{l2} \\ h_2^k \end{bmatrix} = \begin{bmatrix} x_k \\ y_k \\ \frac{\delta h_k^{k+1}}{f} x_{p1}^{k+1} \\ \frac{\delta h_k^{k+1}}{f} y_{p1}^{k+1} \\ x_{k+1} \\ y_{k+1} \\ \frac{\delta h_k^{k+1}}{f} x_{p2}^{k+1} \\ \frac{\delta h_k^{k+1}}{f} y_{p2}^{k+1} \end{bmatrix}. \quad (3)$$

From linear equations (3), it is not difficult to obtain the position of the next frame for the general case. For the convenience of subsequent presentations, we represent the system of equations (3) as

$$As = b. \quad (4)$$

Note that the linear system of equations (3) is singular when there is no height difference between two frames. In order to analyze the singularity of the linear system of equations (3), we simplify it and obtain the following equivalent formula:

$$\begin{aligned} (x_{pn}^{k+1} - x_{pn}^k) \frac{h_n^k}{f} - (x_{p(n+1)}^{k+1} - x_{p(n+1)}^k) \frac{h_{n+1}^k}{f} &= (x_{p(n+1)}^{k+1} - x_{pn}^{k+1}) \delta h_k^{k+1}, \\ (y_{pn}^{k+1} - y_{pn}^k) \frac{h_n^k}{f} - (y_{p(n+1)}^{k+1} - y_{p(n+1)}^k) \frac{h_{n+1}^k}{f} &= (y_{p(n+1)}^{k+1} - y_{pn}^{k+1}) \delta h_k^{k+1}. \end{aligned} \quad (5)$$

It is not difficult to see that it does not only determine landmark height variables h_n^k and h_{n+1}^k from the linear system of equations (5) when the height difference $\delta h_k^{k+1} = 0$.

In order to overcome its singularity, we add the distance information between two sequential frames to assist visual localization, which is provided by the accelerometer in INS. Furthermore, we take into account the constant error and the random walk error of the IMU, the angular line error caused by motion blur and the error of the barometer. Then, the visual-inertial odometer problem is modelled as a stochastic constrain optimization problem. The objective function is formulated as follows:

$$\begin{aligned} \min & \left(\left((x_{k+1} - x_k)^2 + (y_{k+1} - y_k)^2 \right) - \left((d_k^{k+1})^2 - (\delta h_k^{k+1})^2 \right) \right)^2 \\ & + \left(\left((x_{k+1} - x_{k-1})^2 + (y_{k+1} - y_{k-1})^2 \right) - \left((d_{k-1}^{k+1})^2 - (\delta h_{k-1}^{k+1})^2 \right) \right)^2. \end{aligned} \quad (6)$$

For convenience, we denote the above objective function of equation (6) as $f(s)$.

We use the relationship about five landmarks and three frames, which has a similar form to equation (4), as the constraint condition. Due to the measurement error, the

constraint condition can be denoted as

$$A_\varepsilon s = b_\varepsilon, \quad (7)$$

where A_ε includes the vision error and the altimeter error, b_ε is the constant vector with error term. Thus, the odometer problem is reformulated as a random equality-constrained optimization problem. Note that we do not solve the following equivalent nonlinear least-square problem:

$$\min f(s) + \|A_\varepsilon s - b_\varepsilon\|^2. \quad (8)$$

Replacing it, we construct a semi-implicit continuation method with a trust-region technique to directly solve the linearly equality-constrained optimization problem (6)-(7) (see [13, 18, 19] and [20, 21, 22] for the semi-implicit continuation method solving an unconstrained optimization problem and the smallest eigenvalue or generalized eigenvalue problem, respectively).

4.2. Semi-implicit Continuation Method for the Optimization Subproblem

In this subsection, we firstly give a semi-implicit continuation method with a trust-region technique for the linearly equality-constrained optimization subproblem (6)-(7). According to its first-order Karush-Kuhn-Tucker condition

$$\nabla_s L(s, \lambda) = \nabla f(s) + A_\varepsilon^T \lambda = 0, \quad (9)$$

$$A_\varepsilon s = b_\varepsilon, \quad (10)$$

we construct a continuous differential-algebraic gradient flow with index 2 as follows:

$$\frac{ds}{dt} = -\nabla L_s(s, \lambda) = -(\nabla f(s) + A_\varepsilon^T \lambda), \quad (11)$$

$$A_\varepsilon s = b_\varepsilon, \quad (12)$$

where the Lagrangian function is written as

$$L(s, \lambda) = f(s) + \lambda^T (A_\varepsilon s - b_\varepsilon). \quad (13)$$

In order to solve the continuous vector $\lambda(t)$ in (11)-(12), via differentiating its algebraic constraint (12) in variable t and using its differential equation (11), we obtain

$$A_\varepsilon \frac{ds}{dt} = -A_\varepsilon (\nabla f(s) + A_\varepsilon^T \lambda) = -A_\varepsilon \nabla f(s) - A_\varepsilon A_\varepsilon^T \lambda = 0. \quad (14)$$

Assuming that matrix A_ε has a full row rank, from (14), we know that λ satisfies

$$\lambda = -(A_\varepsilon A_\varepsilon^T)^{-1} A_\varepsilon \nabla f(s). \quad (15)$$

Replacing λ in (11) with equation (15), we obtain the ordinary differential gradient flow as follows:

$$\frac{ds}{dt} = -\left(I - A_\varepsilon^T (A_\varepsilon^T)^+\right) \nabla f(s), \quad (16)$$

where $(A_\varepsilon^T)^+ = (A_\varepsilon A_\varepsilon^T)^{-1} A_\varepsilon$ is the generalized inverse of matrix A_ε^T . In other words, we also obtain the continuous projection gradient flow in references [5, 31] via another approach.

We denote

$$P = I - A_\varepsilon^T (A_\varepsilon^T)^+ . \quad (17)$$

Then, it is not difficult to verify $P^2 = P$, i.e., P is a projection matrix and P is an orthogonal projector onto the null space $\mathcal{N}(A)$. Using this property and from (16)-(17), we obtain

$$\begin{aligned} \frac{df(s)}{dt} &= -\nabla f(s)^T \frac{ds}{dt} = -(\nabla f(s))^T P \nabla f(s) = -(\nabla f(s))^T P^2 \nabla f(s) \\ &= -(P \nabla f(s))^T (P \nabla f(s)) = -\|P \nabla f(s)\|_2^2 \leq 0, \end{aligned}$$

namely, the objective function $f(s)$ is decreasing along the solution $s(t)$ of the continuous dynamical system (16). Furthermore, Tanabe [31] and Schropp [28] proves that the solution $s(t)$ tends to s^* as $t \rightarrow \infty$, where s^* satisfies the first-order Karush-Kuhn-Tucker condition (9)-(10). Thus, We can expect to obtain an approximation solution of (6)-(7) via following the trajectory of the ordinary differential dynamical system (16) or the differential-algebraic dynamical system (11)-(12).

For the system of differential-algebraic equations (11)-(12), we look the algebraic equation (12) as a degenerate differential equation. Then, applying the implicit Euler method to the total system, we obtain (see [4, 16, 37] for the implicit Euler method)

$$s_{k+1} = s_k - \Delta t_k (\nabla f(s_{k+1}) + A_\varepsilon^T \lambda_{k+1}), \quad (18)$$

$$A_\varepsilon s_{k+1} = b_\varepsilon. \quad (19)$$

Replacing $\nabla f(s_{k+1})$ with its first-order approximation $\nabla f(s_k) + \Delta t_k \nabla^2 f(s_k)$ and λ_{k+1} with λ_k in (18), respectively, we obtain the predicted variable s_{k+1}^P of the $(k+1)^{th}$ iteration variable s_{k+1} as follows:

$$\left(\frac{1}{\Delta t_k} I + G_k \right) d_k = -p_{gk}, \quad (20)$$

$$s_{k+1}^P = s_k + d_k, \quad (21)$$

where $G_k = \nabla^2 f(s_k)$ and $p_{gk} = \nabla f(s_k) + A_\varepsilon^T \lambda_k$. Since the predicted point s_{k+1}^P will escape from the constraint plane (12), we pull it back via a projection method as follows:

$$\begin{aligned} \min \quad & \|s - s_{k+1}^P\| \\ \text{s.t.} \quad & A_\varepsilon s = b_\varepsilon. \end{aligned} \quad (22)$$

Using the Lagrangian multiplier method (see p. 479, [3]), it is not difficult to obtain the solution of the projection problem (22) as follows:

$$s_{k+1} = s_{k+1}^P + A_\varepsilon^T (A_\varepsilon A_\varepsilon^T)^{-1} (b_\varepsilon - A_\varepsilon s_{k+1}^P). \quad (23)$$

Since s_k is in the constraint plane (12), from equations (21) and (23), we have

$$\begin{aligned}
s_{k+1} &= s_k + d_k + A_\varepsilon^T (A_\varepsilon A_\varepsilon^T)^{-1} (A_\varepsilon s_k - A_\varepsilon s_{k+1}^P) \\
&= s_k + d_k - A_\varepsilon^T (A_\varepsilon A_\varepsilon^T)^{-1} A_\varepsilon d_k \\
&= s_k + \left(I - A_\varepsilon^T (A_\varepsilon A_\varepsilon^T)^{-1} A_\varepsilon \right) d_k \\
&= s_k + P d_k,
\end{aligned} \tag{24}$$

where projection matrix P is defined by (17).

Using the implicit relationship (15) between the Lagrangian multiplier $\lambda(t)$ and the differential variable $s(t)$, we obtain the Lagrangian multiplier at the $(k+1)^{th}$ iteration

$$\lambda_{k+1} = - (A_\varepsilon A_\varepsilon^T)^{-1} A_\varepsilon \nabla f(s_{k+1}). \tag{25}$$

Replacing equation (25) into $p_{g_k} = \nabla f(s_k) + A_\varepsilon^T \lambda_k$, we have

$$p_{g_k} = \nabla f(s_k) + A_\varepsilon^T \lambda_k = \left(I - A_\varepsilon^T (A_\varepsilon A_\varepsilon^T)^{-1} A_\varepsilon \right) \nabla f(s_k) = P g_k, \tag{26}$$

where $g_k = \nabla f(s_k)$.

Another issue is how to adaptively adjust the time-stepping length Δt_k every iteration. We borrow it from the trust-region method for its robust global convergence property and fast local convergence property (see pp. 561-593, [30]). Since variable s_k is feasible, i.e. it always stay in the constraint plane (12) every iteration, the objective function $f(s)$ is a suitable merit function for adjusting the time stepping length Δt_k as we use a trust-region technique.

When a trust-region technique is selected, we need to construct an local approximation model around variable s_k . According to the traditional approach, we adopt a quadratic model as follows:

$$q_k(s) = (s - s_k)^T \nabla f(s_k) + \frac{1}{2} (s - s_k)^T \nabla^2 f(s_k) (s - s_k). \tag{27}$$

Now, based on the following measurement ratio

$$\rho_k = \frac{f(s_k) - f(s_{k+1})}{q_k(s_k) - q_k(s_{k+1})}, \tag{28}$$

we give an adaptive adjustment time-stepping length formula

$$\Delta t_{k+1} = \begin{cases} \gamma_1 \Delta t_k, & \text{if } 0 \leq |1 - \rho_k| \leq \eta_1, \\ \Delta t_k, & \text{if } \eta_1 < |1 - \rho_k| < \eta_2, \\ \gamma_2 \Delta t_k, & \text{if } |1 - \rho_k| \geq \eta_2, \end{cases} \tag{29}$$

where the constants are selected as $0 < \gamma_2 \leq 1/2$, $1 < \gamma_1 \leq 2$, $0 < \eta_1 \leq 0.25$ and $0.75 < \eta_2 < 1$ according to numerical experiments. The specific algorithm steps are shown in algorithm 1.

Algorithm 1 Semi-implicit Continuation Method with Trust-region Technique for Linearly Equality-constrained Optimization

Input:

An objective function: $f(s)$,
 and the linear constraint: $A_\varepsilon s = b_\varepsilon$,
 and the minimum absolute gradient bound of Lagrangian function $L(s, \lambda) = f(s) + \lambda^T (A_\varepsilon s - b)$: δ_ε .

Output:

The optimal approximation solution s^* .

- 1: Initialize a point s_0 and the parameter Δt_0 .
 - 2: Choose constants $\eta_a, \eta_1, \eta_2, \gamma_1, \gamma_2$ to satisfy
 $0 < \eta_a < \eta_1 \leq 1/2 < \eta_2 < 1$ and $0 < \gamma_2 < 1 < \gamma_1$,
 such as $\eta_a = 10^{-6}$, $\eta_1 = 0.25$, $\eta_2 = 0.75$ and $\gamma_1 = 2$, $\gamma_2 = 0.5$.
 - 3: $k \leftarrow 0$
 - 4: Compute $f_0 = f(s_0)$, $g_0 = \nabla f(s_0)$, $p_{g_0} = \nabla_s L(s_0, \lambda_0) = g_0 + A_\varepsilon^T \lambda_0$ and $G_0 = \nabla_s^2 L(s_0, \lambda_0) = \nabla^2 f(s_0)$, where the Lagrangian multiplier $\lambda_0 = -(A_\varepsilon A_\varepsilon^T)^{-1} A_\varepsilon g_0$.
 - 5: **while** $\|g_k\| > \delta_\varepsilon$ **do**
 - 6: **if** $1/\Delta t_k I + G_k \succ 0$ and $(1/\Delta t_k I + G_k - P^T G_k P) \succ 0$ **then**
 - 7: Compute d_k based on equation (20).
 - 8: Let $s_{k+1}^P = s_k + d_k$ and project s_{k+1}^P to the constraint plane $A_\varepsilon s = b_\varepsilon$ by solving problem (22), and obtain s_{k+1} which is given by equation (23).
 - 9: Compute $f_{k+1} = f(s_{k+1})$ and the measurement ratio ρ_k based on equations (27)-(28).
 - 10: **else**
 - 11: $\rho_k = -1$.
 - 12: **end if**
 - 13: **if** $\rho_k \leq \eta_a$ **then**
 - 14: $s_{k+1} = s_k$.
 - 15: **else**
 - 16: Accept s_{k+1} and compute $g_{k+1} = \nabla f(s_{k+1})$, $G_{k+1} = \nabla^2 f(s_{k+1})$, $\lambda_{k+1} = (A_\varepsilon A_\varepsilon^T)^{-1} A_\varepsilon g_{k+1}$, and the projection gradient $p_{g_{k+1}} = g_{k+1} + A_\varepsilon^T \lambda_{k+1}$.
 - 17: **end if**
 - 18: Adjust the time-stepping length Δt_{k+1} based on the trust-region technique (29).
 - 19: Update $\lambda_k \leftarrow \lambda_{k+1}$, $s_k \leftarrow s_{k+1}$, $f_k \leftarrow f_{k+1}$, $g_k \leftarrow g_{k+1}$, $G_k \leftarrow G_{k+1}$, $p_{g_k} \leftarrow p_{g_{k+1}}$ and $k \leftarrow k + 1$.
 - 20: **end while**
-

4.3. Convergence Analysis of Semi-implicit Continuation Method for optimization sub-problem

In this subsection, we give the local and the global convergence properties of the semi-implicit continuation method for the linearly equality-constrained optimization subproblem (i.e. Algorithm 1). Firstly, we give an estimation of upper bounds for the quadratic model $q_k(s_{k+1})$ which is similar result of the trust-region method for unconstrained optimization problem [25].

Lemma 4.1. *Assume that the quadratic model $q_k(s)$ is defined by (27) and d_k is solved by equations (20)-(23). If $(1/\Delta t_k I + G_k) \succ 0$ and $(1/\Delta t_k I + G_k - P^T G_k P) \succ 0$ for some $\Delta t_k > 0$, where projection matrix P is given by equation (17), we have an estimation of lower bounds for the predicted reduction $Pred_k = q_k(s_k) - q_k(s_k + Pd_k)$ as follows:*

$$Pred_k \geq \frac{1}{2} \|p_{g_k}\| \min \{ \|Pd_k\|, \|p_{g_k}\|/\|G_k\| \}, \quad (30)$$

where $p_{g_k} = \nabla_s L(s_k, \lambda_k) = \nabla f(s_k) + A_\varepsilon^T \lambda_k$ and the Lagrange multiplier λ_k is determined by equation (25).

Proof. Assume that d_k is the solution of equation (20). Then, we have

$$\begin{aligned} q_k(s_k) - q_k(s_k + Pd_k) &= -\frac{1}{2} d_k^T P^T G_k P d_k - g_k^T P d_k \\ &= -\frac{1}{2} d_k^T P^T G_k P d_k + p_{g_k}^T (\mu_k I + G_k)^{-1} p_{g_k} \\ &= \frac{1}{2} p_{g_k}^T (\mu_k I + G_k)^{-1} p_{g_k} + \frac{1}{2} d_k^T (-P^T G_k P + \mu_k I + G_k) d_k, \end{aligned} \quad (31)$$

where we denote $\mu_k = 1/\Delta t_k$. From the above equality (31), $(\mu_k I + G_k) \succ 0$ and selecting a constant μ_{lb} such that $\mu_{lb} = \min \{0, -\lambda_{min}(G_k - P^T G_k P)\}$, where $\lambda_{min}(G_k - P^T G_k P)$ is the smallest eigenvalue of matrix $(G_k - P^T G_k P)$, we obtain

$$\begin{aligned} q_k(s_k) - q_k(s_{k+1}) &\geq \frac{1}{2} p_{g_k}^T (\mu_k I + G_k)^{-1} p_{g_k} + \frac{1}{2} (\mu_k - \mu_{lb}) \|d_k\|^2 \\ &\geq \frac{1}{2} \left(\frac{1}{\mu_k + \|G_k\|} \|p_{g_k}\|^2 + (\mu_k - \mu_{lb}) \|d_k\|^2 \right). \end{aligned} \quad (32)$$

Now we consider the properties of the function

$$\varphi(\mu) \equiv \mu \|d_k\|^2 + \frac{1}{\mu + \mu_{lb} + \|G_k\|} \|p_{g_k}\|^2. \quad (33)$$

It is not difficult to know that the function $\varphi(\mu)$ is convex when $(\mu + \|G_k\|) > 0$, since $\varphi''(\mu) = 2\|p_{g_k}\|^2/(\mu + \mu_{lb} + \|G_k\|)^3 \geq 0$. Thus, the function $\varphi(\mu)$ attains its minimizer $\varphi(\mu_{min})$ when μ_{min} satisfies $\varphi'(\mu_{min}) = 0$ and $\mu \geq -(\mu_{lb} + \|G_k\|)$, i.e.

$$\varphi(\mu_{min}) = 2\|p_{g_k}\| \|d_k\| - (\mu_{lb} + \|G_k\|) \|d_k\|^2, \quad (34)$$

when

$$\mu_{min} = \|p_{g_k}\|/\|d_k\| - \mu_{lb} - \|G_k\|, \text{ and } \mu_{min} > -(\mu_{lb} + \|G_k\|). \quad (35)$$

We prove the property (30) by distinguishing two cases separately, namely μ_{min} is nonnegative or negative. When $\|p_{g_k}\|/\|d_k\| \geq (\mu_{lb} + \|G_k\|)$, from (35), we have $\mu_{min} \geq 0$. For this case, combining $\mu_k \geq \mu_{lb}$ with equations (32)–(35), we obtain

$$\begin{aligned} q_k(s_k) - q_k(s_k + Pd_k) &\geq (\mu_k - \mu_{lb})\|d_k\|^2 + \frac{1}{\mu_k + \|G_k\|}\|g_k\|^2 = \varphi(\mu_k - \mu_{lb}) \geq \varphi(\mu_{min}) \\ &= \frac{1}{2}(\|p_{g_k}\|\|d_k\| + (\|p_{g_k}\|\|d_k\| - (\mu_{lb} + \|G_k\|)\|d_k\|^2)) \geq \frac{1}{2}\|p_{g_k}\|\|d_k\|. \end{aligned} \quad (36)$$

The other case is $\|p_{g_k}\|/\|d_k\| < (\mu_{lb} + \|G_k\|)$, which gives $\mu_{min} < 0$ from (35). Since the function $\varphi(\mu)$ is monotonically increasing for all $\mu \geq 0$ when $\|p_{g_k}\|/\|d_k\| < (\mu_{lb} + \|G_k\|)$, from equations (32)–(33), we obtain

$$\begin{aligned} q_k(s_k) - q_k(s_k + Pd_k) &\geq \frac{1}{2}\left((\mu_k - \mu_0)\|d_k\|^2 + \frac{1}{\mu_k + \|G_k\|}\|p_{g_k}\|^2\right) \\ &= \frac{1}{2}\varphi(\mu_k - \mu_{lb}) \geq \frac{1}{2}\varphi(0) = \frac{1}{2}\|p_{g_k}\|^2/\|G_k\|. \end{aligned} \quad (37)$$

Combining (36) and (37), we get

$$q_k(s_k) - q_k(s_k + Pd_k) \geq \frac{1}{2}\|p_{g_k}\| \min\{\|p_{g_k}\|/\|G_k\|, \|d_k\|\}. \quad (38)$$

Since s_{k+1} is the projection of $s_{k+1}^P = s_k + d_k$ in a convex set $C_s = \{s : A_\varepsilon s = b_\varepsilon\}$, according to Projection Theorem (see Proposition 1.1.4, p. 19 [3]), we have

$$\|Pd_k\| = \|Ps_{k+1}^P - Ps_k\| \leq \|s_{k+1}^P - s_k\| = \|d_k\|. \quad (39)$$

Using inequality (39) in equation (38), we obtain an estimation (30), which proves the lemma. \square

In order to prove that p_{g_k} tends to zero, we also use the following result about the lower bound estimation of the time-stepping length Δt_k when $\|p_{g_k}\| \geq \delta_{p_g} > 0$.

Lemma 4.2. *Assume that the level set of the twice continuously differentiable function $f : \mathbf{R}^n \rightarrow \mathbf{R}$ in the linear constraint plane (12) is bounded, i.e. $L_f = \{s : f(s) \leq f(s_0), A_\varepsilon s = b_\varepsilon\}$ is bounded. Furthermore, assume that there exists a positive constant δ_g such that*

$$\|p_{g_k}\| \geq \delta_{p_g} > 0, \quad k = 1, 2, \dots \quad (40)$$

are satisfied, where p_{g_k} are generated by Algorithm 1. Then, it exists a positive $\delta_{\Delta t}$ such that the time-stepping length

$$\Delta t_k \geq \delta_{\Delta t} > 0, \quad k = 1, 2, \dots \quad (41)$$

are satisfied, where Δt_k is adaptively adjusted by formula (29).

Proof. Since the level set L_f is bounded, according to Proposition A.7 in pp. 754-755 of reference [3], L_f is closed. Then, there exists two positive constants M_{p_g} and M_G such that

$$\|p_{gk}\| \leq M_{p_g}, \|G_k\| \leq M_G, k = 1, 2, \dots \quad (42)$$

are satisfied, respectively. Selecting a positive $\delta_{\Delta_0} = 1/(2M_G)$, we have $(1/\Delta t_k I + G_k) \succ 0$ and $(1/\Delta t_k I + G_k - P^T G_k P) \succ 0$ when $\Delta t_k \leq \delta_{\Delta_0}$, where projection matrix P is given by equation (17).

From equations (28), (50) and the reduction estimation (30) of the quadratic model (see Lemma 4.2), when $\Delta t_k \leq \delta_{\Delta_0}$, we obtain the estimation of the measurement ratio

$$\begin{aligned} |\rho_k - 1| &= \left| \frac{(f(s_k) - f(s_k + Pd_k)) - (q_k(s_k) - q_k(s_k + Pd_k))}{q_k(s_k) - q_k(s_k + Pd_k)} \right| \\ &= \left| \frac{1/2(Pd_k)^T (G_k - \nabla^2 f(\bar{s}_k)) (Pd_k)}{q_k(s_k) - q_k(s_k + Pd_k)} \right| \leq \frac{M_G \|Pd_k\|^2}{|q_k(s_k) - q_k(s_k + Pd_k)|} \\ &\leq \frac{M_G \|Pd_k\|^2}{\frac{1}{2} \|p_{gk}\| \min\{\|Pd_k\|, \|p_{gk}\|/\|G_k\|\}} \leq \frac{2M_G \|Pd_k\|^2}{\delta_{p_g} \min\{\|Pd_k\|, \delta_{p_g}/M_G\}}. \end{aligned} \quad (43)$$

In the above third inequality and the last inequality, we use the Cauchy-Schwartz inequality $|x^T y| \leq \|x\| \|y\|$ and the lower bound assumption (40) of the projection gradient p_{gk} .

Selecting a positive constant $\delta_{\Delta_1} = \min\{\delta_{p_g}/M_G, \eta_1 \delta_{p_g}/(2M_G)\}$, when $\Delta t_k \leq \delta_{\Delta_0}$ and $\|Pd_k\| \leq \delta_{\Delta_1}$, from equation (43), we have

$$|\rho_k - 1| \leq \eta_1, \quad (44)$$

which means that the predicted point $s_{k+1} = s_k + Pd_k$ is accepted and the time-stepping length Δt_{k+1} is enlarged according to the time-stepping adjustment formula (29).

From equations (20) and (50), when $\Delta t_k \leq \delta_{\Delta_2} = \min\{1/\delta_{\Delta_0}, 1/(M_{p_g}/\delta_{\Delta_1} + M_G)\}$, we have

$$\begin{aligned} \|d_k\| &= \left\| \left(\frac{1}{\Delta t_k} I + G_k \right)^{-1} p_{gk} \right\| \\ &\leq \frac{\|p_{gk}\|}{1/\Delta t_k - \|G_k\|} \leq \frac{M_{p_g}}{1/\Delta t_k - M_G} \leq \delta_{\Delta_1}, \end{aligned} \quad (45)$$

which means that inequality (44) is satisfied according to the projection property (39) (i.e., $\|Pd_k\| \leq \|d_k\|$).

Assume that K is the first index such that $\Delta t_K \leq \delta_{\Delta_2}$ is satisfied. Then, according to the projection property (39), inequalities (45) and (44), we know that $|\rho_K - 1| \leq \eta_1$, which means that $s_K + Pd_K$ is accepted and the time-stepping length Δt_{K+1} is enlarged according to the time-stepping adjustment formula (29). Consequently, the

time-stepping length $\Delta t_k \geq \min\{\gamma_1 \delta_{\Delta_2}, \Delta t_K\}$ when $k \geq K$, which proves the lemma. \square

Using the results of Lemma 4.1 and Lemma 4.2, we can prove the global convergence property of Algorithm 1 for a linearly equality-constrained optimization sub-problem.

Theorem 4.1. *Assume that the level set of the twice continuously differentiable function $f(s)$ in the linear constraint plane (12) is bounded, i.e. $L_f = \{s : f(s) \leq f(s_0), A_\varepsilon s = b_\varepsilon\}$ is bounded. Then, $\lim_{k \rightarrow \infty} \inf \|p_{g_k}\| = 0$, where $p_{g_k} = \nabla f(s_k) + A_\varepsilon^T \lambda_k$ and s_k, λ_k are generated by Algorithm 1.*

Proof. We will prove it by contradiction. Assume that the conclusion is not true. Then it exists a positive constant δ_{p_g} such that

$$\|p_{g_k}\| \geq \delta_{p_g} > 0, k = 1, 2, \dots \quad (46)$$

are satisfied. According to Algorithm 1, we know that it exists an infinite subsequent k_i such that trial step Pd_{k_i} are accepted, i.e., $\rho_{k_i} \geq \eta_a$, which gives

$$f_0 - \lim_{k \rightarrow \infty} f_k = \sum_{k=0}^{\infty} (f_k - f_{k+1}) \geq \eta_a \sum_{k_i=0}^{\infty} (q_k(s_{k_i}) - q_k(s_{k_i} + Pd_{k_i})), \quad (47)$$

where Pd_k is computed by equations (20) and (24). Using the bounded assumption of the objective function $f(s)$ in the level set L_f for inequality (47), we know

$$\lim_{k \rightarrow \infty} (q_k(s_{k_i}) - q_k(s_{k_i} + Pd_{k_i})) = 0. \quad (48)$$

From the result of Lemma 4.1, i.e. inequality (30), and equation (48), we get

$$\lim_{k_i \rightarrow \infty} \|p_{g_{k_i}}\| \min \left\{ \|p_{g_{k_i}}\| / \|G_{k_i}\|, \|Pd_{k_i}\| \right\} = 0, \quad (49)$$

where $G_{k_i} = \nabla^2 f(s_{k_i})$.

According to the bounded assumption of the level set L_f , there exists two positive constants M_{p_g} and M_G such that

$$\|p_{g_k}\| \leq M_{p_g}, \|G_k\| \leq M_G, k = 1, 2, \dots \quad (50)$$

are satisfied, respectively. From equation (50) and inequalities (46) and (50), for the subsequent $\{k_i\}$ of accepted trial steps, we obtain

$$\lim_{k_i \rightarrow \infty} \|Pd_{k_i}\| = 0. \quad (51)$$

According to the bounded assumption of p_{g_k} (46) and inequality (50), from the result of Lemma 4.2, we know that it exists a positive constant δ_{Δ} such that

$$\Delta t_k \geq \delta_{\Delta} > 0, k = 1, 2, \dots \quad (52)$$

are satisfied.

From equation (20) and using the property $P^2 = P$ of projection matrix P which is defined by (17), we obtain

$$Pd_{k_i} = \left(P \left(\frac{1}{\Delta t_{k_i}} I + G_{k_i} \right)^{-1} P \right) p_{g_{k_i}}, \quad (53)$$

which gives

$$\begin{aligned} p_{g_{k_i}}^T Pd_{k_i} &= p_{g_{k_i}}^T \left(P \left(\frac{1}{\Delta t_{k_i}} I + G_{k_i} \right)^{-1} P \right) p_{g_{k_i}} \\ &= p_{g_{k_i}}^T \left(\frac{1}{\Delta t_{k_i}} I + G_{k_i} \right)^{-1} p_{g_{k_i}} \geq \|p_{g_{k_i}}\|^2 \frac{1}{1/\delta_{\Delta t} - M_G}. \end{aligned} \quad (54)$$

Using the Cauchy-Schwartz inequality $|x^T y| \leq \|x\| \|y\|$, from equation (46), we have

$$\frac{1}{1/\delta_{\Delta t} - M_G} \|p_{g_{k_i}}\|^2 \leq |p_{g_{k_i}}^T Pd_{k_i}| \leq \|p_{g_{k_i}}\| \|Pd_{k_i}\| \quad (55)$$

which gives

$$\|p_{g_{k_i}}\| \leq (1/\delta_{\Delta t} - M_G) \|Pd_{k_i}\|. \quad (56)$$

From inequality (56) and equation (51), we obtain

$$\lim_{k_i \rightarrow \infty} \|p_{g_{k_i}}\| = 0, \quad (57)$$

which contradicts the lower bound assumption (46). Therefore, we prove the conclusion of the theorem. \square

4.4. Visual-Inertial Algorithm Descriptions

The proposed visual-inertial odometer method is described in Algorithm 2. To convention, the input INS reading has been pre-calibrated and the camera intrinsic parameters have been obtained. In algorithm 2, the positions of the $(k-1)^{th}$ and k^{th} frame have been determined before, denoted as Pc_{k-1} and Pc_k . And let $dist_{k-1}^{k+1}$ and $dist_k^{k+1}$ be the distances between the previous two frames and the $(k+1)^{th}$ frame, respectively, which are measured by INS. Similarly, let δh_{k-1}^{k+1} and δh_k^{k+1} present the altitude differences between the previous two frames and the $(k+1)^{th}$ frame, respectively, which are obtained by altimeter. Then, we use feature matching to obtain the landmarks' locations in frame coordinate system. Finally, the $(k+1)^{th}$ frame position is determined through solving the linearly equality-constrained optimization problem (6)-(7), which is solved by Algorithm 1. After a number of iterations, the aircraft trajectory is determined.

We just consider the relationships between frames and landmarks, and the visual-inertial method have not loop closure detection. Therefore, algorithm 1 has good real-time performance. Additionally, the proposed algorithm tolerates a certain level of altitude error as we take into account the random error of each component.

Algorithm 2 Visual-inertial Odometry Algorithm**Input:**

the $(k-1)^{th}$ and k^{th} frames' locations Pc_{k-1} , Pc_k , respectively; the distances $dist_{k-1}^{k+1}$, $dist_k^{k+1}$ between the previous two frames and the $(k+1)^{th}$ frame, respectively; and the altitude differences δh_{k-1}^{k+1} , δh_k^{k+1} between the previous two frames and the $(k+1)^{th}$ frame, respectively.

Output:

The next frame location Pc_{k+1} .

- 1: **for** a number of iterations **do**
- 2: Determining the landmarks \leftarrow matching the ORB feature in the $(k+1)^{th}$ frame and the ORB features in the previous two frames, respectively.
- 3: **end for**
- 4: **for** a number of iterations **do**
- 5: Obtain the landmarks' locations in the $(k+1)^{th}$ frame coordinate system and in previous frame coordinate system.
- 6: **end for**
- 7: Get matrix A_e in equation (7).
- 8: Solve the equality-constrained optimization problem (6)-(7) with Algorithm 1.
- 9: **return** Pc_{k+1} .

5. Simulation Results

In order to illustrate the effect of the proposed algorithm, we compare the localization accuracy of our algorithm and the pure inertial navigation on the same trajectory. The aircraft sets off at some point in the equator and then flies along the equatorial plane for an hour. According to the given condition from the industry, we assume that the aircraft flies an hour at an altitude of 1200 meters with speed 235 meters per second. We also consider the line-of-sight angular error to be less than 0.2 degrees, the random error of altimeter and the altimeter error associated with the distance. The specific key parameters are shown in table 1.

Table 1: Aircraft key performance parameters

Description	Parameter value
Flight altitude of the aircraft	1000 ~ 1500 meters
Flight speed of the aircraft	210 ~ 260 meters per second
The line-of-sight angular error of landmarks	$\leq 0.2^\circ$
The random error of altimeter	one meter (variance σ value)
The altimeter error related to flight distance	$< \text{Flight distance} * 0.0001$
Horizontal attitude error of INS	$< 0.06^\circ$
The heading error of INS	$< 0.4^\circ$
Required accuracy of localization	< 900 meters per hour

The simulation error of the proposed method is shown in figure 4. Figure 5 presents the comparison between our method and the pure inertial navigation method. The vertical axis represents the error between the real positioning location and the ideal trajectory. The horizontal axis is about the flying time. Owing to the long-time high-speed flight, the pure INS method does not work well. From Figure 5, we find that the error of inertial navigation is more than 9 kilometers per hour, and our method which combines the advantages of inertial navigation and visual odometry effectively suppress the rapid propagation of errors. The accuracy of proposed method is only slightly less than 300 meters. The effect of our proposed method has a noticeable improvement and its accuracy meets the navigation accuracy requirements.

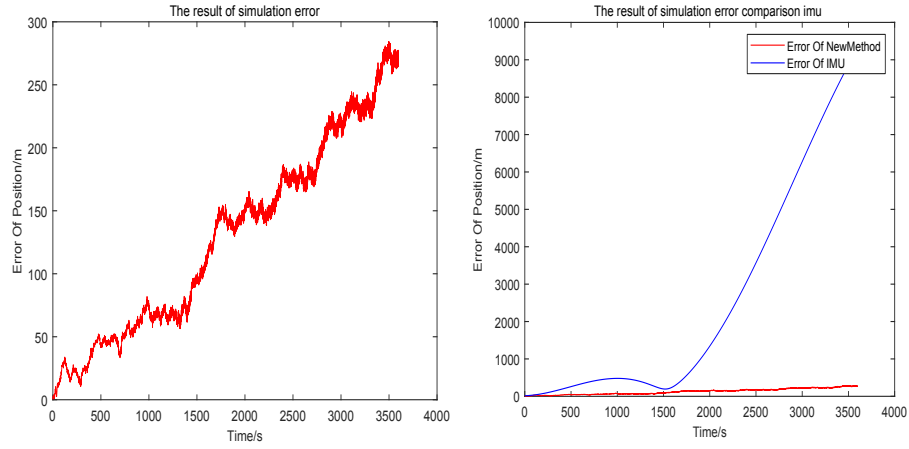


Figure 4: The result of proposed simulation position-
Figure 5: The comparison between proposed method and pure INS.

6. Conclusion and Future Work

The proposed algorithm combining the visual odometer to assist INS effectively utilizes the complementarity of two methods. It avoids the rapid accumulation of errors in an inertial navigation method, and has no problem of scale ambiguity. Since there is no the loop closure detection, the proposed algorithm has good real-time performance compared to other vision-based methods. Currently, we only consider the horizontal flight with small variation in yaw angle. When the roll angle and the pitch angle frequently change, the proposed method do not work very well. Thus, the proposed algorithm is only applicable to the four DOF motion. In order to solve the localization in this six DOF flight scenario, we will design a more robust algorithm for full freedom navigation base on the newly proposed method in the future.

Financial and Ethical Disclosures

- Funding: This study was funded by Grant 61876199 from National Natural Science Foundation of China, Grant YBWL2011085 from Huawei Technologies Co., Ltd., and Grant YJCB2011003HI from the Innovation Research Program of Huawei Technologies Co., Ltd..
- Conflict of Interest: The authors declare that they have no conflict of interest.

Acknowledgments The first author is grateful to Professor Ya-Xiang Yuan and this work is dedicated to him on the occasion of his 60th birthday.

References

- [1] N. Ahmad, R. Ghazilla, N. Khairi and V. Kasi, *Reviews on various inertial measurement unit (IMU) sensor applications*, International Journal of Singal Processing Systems, **1** (2), pp. 256-262, 2013.
- [2] A. Anwar, W. Lin, X. Deng, J. Qiu and H. Gao, *Quality inspection of Remote Radio Units using depth-free image-based visual servo with acceleration command*, IEEE Transactions on Industrial Electronics, **66** (10), pp. 8214-8223, 2019.
- [3] D. P. Bertsekas, *Nonlinear Programming (3rd Edition)*, Tsinghua University Press, 2018.
- [4] U. M. Ascher and L. R. Petzold, *Computer Methods for Ordinary Differential Equations and Differential-Algebraic Equations*, SIAM, Philadelphia, PA, 1998.
- [5] A. A. Brown and M. C. Bartholomew-Biggs, *ODE versus SQP methods for constrained optimization*, Journal of Optimization and Theory Applications, **62** (3), pp. 371-386, 1989.
- [6] G. Conte and P. Doherty, *An integrated UAV navigation system based on aerial image matching*, Proceedings of IEEE Aerospace Conference, pp. 1-10, 2008.
- [7] G. Conte and P. Doherty, *Vision-based unmanned aerial vehicle navigation using geo-reference information*, EURASIP Journal on Advances in Signal Processing, pp. 1-18, 2009, <https://doi.org/10.1155/2009/387308>.
- [8] F. Caballero, L. Merino, J. Ferruz and A. Ollero, *Vision-based odometry and SLAM for medium and high altitude flying UAVs*, Journal of Intelligent and Robotic Systems, **54** (1-3), pp. 137-161, 2009.
- [9] G. Ellingson, K. Brink, T. McLain, *Relative visual-inertial odometry for fixed-wing aircraft in GPS-denied environments*, 2018 IEEE/ION Position, Location and Navigation Symposium (PLANS), pp. 786-792, 2018.
- [10] J. Engel and D. Cremers, *Scale-aware navigation of a low-cost quadcopter with a monocular camera*, Robotics and Autonomous Systems (RAS), **62** (11), pp. 1646-1656, 2014.

- [11] Y. Fei, C. Lv and Q. Dong, *A novel robust H_∞ filter based on krein space theory in the SINS/CNS attitude reference system*, *Sensors*, **16** (3): 396, pp. 1-15, 2016.
- [12] A.V. Fiacco and G. P. McCormick, *Nonlinear programming: Sequential Unconstrained Minimization Techniques*, SIAM, 1990.
- [13] B.S. Goh, *Approximate greatest descent methods for optimization with equality constraints*, *Journal of Optimization Theory and Applications* **148** (3), pp. 505-527.
- [14] M. S. Grewal, L. R. Weill and A. P. Andrews, *Global Positioning Systems, Inertial Navigation and Integration*, Wiley Interdisciplinary Reviews Computational Statistics, **3** (4), pp. 739-744, 2011.
- [15] R. Hartley and A. Zisserman, *Multiple View Geometry in Computer Vision (2nd edition)*, New York, Cambridge University Press, 2003.
- [16] E. Hairer and G. Wanner, *Solving Ordinary Differential Equations II, Stiff and Differential-Algebraic Problems*, 2nd ed., Springer-Verlag, Berlin, 1996.
- [17] L. Kneip, M. Chli and R. Siegwart, *Robust real-time visual odometry with a single camera and an IMU*, Proc. of the British Machine Vision Conference (BWVC), 2011, <https://doi.org/10.5244/C.2516>.
- [18] X. L. Luo, L. Z. Liao and H. W. Tam, *Convergence analysis of Levenberg-Marquardt methods*, *Optimization Methods and Software*, **22** (4), pp. 659-678, 2007.
- [19] X. L. Luo, C. Kelley, L. Z. Liao and H. Tam, *Combining trust-region techniques and rosenbrock methods to compute stationary points*, *Journal of Optimization Theory and Applications*, **140** (2), pp. 265-286, 2009.
- [20] S.-T. Liu and X.-L. Luo, *A method based on Rayleigh quotient gradient flow for extreme and interior eigenvalue problems*, *Linear Algebra and its Applications*, **432** (7), pp. 1851-1863, 2010.
- [21] X.-L. Luo, *A dynamical method of DAEs for the smallest eigenvalue problem*, *Journal of Computational Science*, **3** (3), pp. 113-119, 2012.
- [22] X.-L. Luo, J.-R. Lin and W.-L. Wu, *A prediction-correction dynamic method for large-scale generalized eigenvalue problems*, *Abstract and Applied Analysis*, Article ID 845459, pp. 1-8, <http://dx.doi.org/10.1155/2013/845459>, 2013.
- [23] A. I. Mourikis and S. I. Roumeliotis, *A multi-state constraint Kalman filter for vision-aided inertial navigation*, *IEEE International Conference on Robotics and Automation*, pp. 3565-3572, 2007.
- [24] H. Oleynikova, M. Burri S. Lynen and R. Siegwart, *Real-time visual-inertial localization for aerial and ground robots*, 2015 IEEE/RSJ International Conference on Intelligent Robots and Systems (IROS), pp. 3079-3085, 2015.

- [25] M. J. D. Powell, *Convergence properties of a class of minimization algorithms*, in: O.L. Mangasarian, R. R. Meyer and S. M. Robinson, eds., *Nonlinear Programming 2*, Academic Press, New York, 1975, pp. 1-27.
- [26] M. Quan, S. Piao, M. Tan, and S. Huang, *Accurate monocular visual-inertial SLAM using a map-assisted EKF approach*, *IEEE Access*, **7**, pp. 34289-34300, 2019.
- [27] E. Rublee, V. Rabaud, K. Konolige, and G. Bradski, *Orb: an efficient alternative to sift or surf*, *IEEE International Conference on Computer Vision (ICCV)*, pp. 2564-2571, 2011.
- [28] J. Schropp, *A dynamical systems approach to constrained minimization*, *Numerical Functional Analysis and Optimization*, **21**(3-4), pp. 537-551, 2000.
- [29] T.J. Steiner, R.D. Truax and K. Frey, *A vision-aided inertial navigation system for agile high-speed flight in unmapped environments*, *Proceedings of IEEE Aerospace Conference*, pp. 1-10, 2017.
- [30] W.Y. Sun and Y.-X. Yuan, *Optimization Theory and Methods*, Springer, 2006.
- [31] K. Tanabe, *A geometric method in nonlinear programming*, *Journal of Optimization Theory and Applications*, **30** (2), pp. 181-210, 1980.
- [32] D. Titterton and J. Weston, *Strapdown inertial navigation technology (2nd edition)*, *IEEE Aerospace and Electronic Systems Magazine*, **20** (7), pp. 1-6, 2004.
- [33] O. J. Woodman, *An introduction to inertial navigation*, Research report, No. 696, University of Cambridge, 2007.
- [34] M. Warren and B. Upcroft, *High altitude stereo visual odometry*, *Proceedings of Robotics: Science and Systems IX*, pp. 1-8, 2013.
- [35] L. Yang, B. Li and L. Ge, *A novel sins/cns integrated navigation algorithm used in a ballistic missile*, *International Journal of Security and Its Applications*, **9** (9), pp. 65-76, 2015.
- [36] G. Yan, *Precise Strapdown Inertial Navigation System (PSINS) Toolbox for MATLAB (Version 2.0)*, [Software]. Available from http://blog.sina.com.cn/s/blog_40edfdc90101heg0.html.
- [37] D. G. Liu and J. G. Fei, *Digital Simulation Algorithms for Dynamic Systems* (in Chinese), Science Press, Beijing, 2000.
- [38] J. Zhang and S. Singh, *Visual-inertial combined odometry system for aerial vehicles*, *Journal of Field Robotics*, **32** (8), pp. 1043-1055, 2015.